Therapeutic Targeting of Tumor-Stromal HGF-cMET Signaling in an Organotypic Triple Negative Breast Tumor Model

Sunil Singh[1], Astha Lamichhane[1], Pouria Rafsanjani Nejad[1], Jacob Heiss[1], Hannah Baumann[2], Ravindra Gudneppanavar[3], Nic D. Leipzig[2], Michael Konopka[3], Gary D. Luker[4], and Hossein Tavana[1*]

[1] Department of Biomedical Engineering, The University of Akron, Akron, Ohio, USA

[2] Department of Chemical, Biomolecular, and Corrosion Engineering, The University of Akron, Akron, Ohio, USA

[3] Department of Chemistry, The University of Akron, Akron, Ohio, USA

[4] Departments of Radiology, Microbiology and Immunology, Biomedical Engineering, University of Michigan, Ann Arbor, Michigan, USA

Running title: Targeting tumor-stromal interactions in a 3D TNBC tumor model

*Corresponding author:
Hossein Tavana, Ph.D., P. Eng.
260 S. Forge St., Akron, OH 44325
Tel: (330) 972-6031; Fax: (330) 374-8834
E-mail: tavana@uakron.edu

Disclosure of Potential Conflicts of Interest: Authors declare no conflict of interest.

Abstract

The tumor microenvironment (TME) promotes proliferation, drug resistance, and invasiveness of cancer cells. Therapeutic targeting of the TME is an attractive strategy to improve outcomes for patients, particularly in aggressive cancers such as triple negative breast cancer (TNBC) that have a rich stroma and limited targeted therapies. However, lack of preclinical human tumor models for mechanistic understanding of tumor-stromal interactions has been an impediment to identify effective treatments against the TME. To address this need, we developed a three-dimensional (3D) organotypic tumor model to study interactions of patient-derived cancer-associated fibroblasts (CAFs) with TNBC cells and explore potential therapy targets. We found that CAFs predominantly secreted hepatocyte growth factor (HGF) and activated MET receptor tyrosine kinase in TNBC cells. This tumor-stromal interaction promoted invasiveness, epithelial-to-mesenchymal transition, and activities of multiple oncogenic pathways in TNBC cells. Importantly, we established that TNBC cells become resistant to monotherapy and demonstrated a design-driven approach to select drug combinations that effectively inhibit pro-metastatic functions of TNBC cells. Our study also showed that HGF-MET from lung fibroblasts promotes colony formation by TNBC cells, suggesting that blocking HGF-MET signaling potentially could target both primary TNBC tumorigenesis and lung metastasis. Overall, we established the utility of our organotypic tumor model to identify and therapeutically target specific mechanisms of tumor-stromal interactions in TNBC toward the goal of developing targeted therapies against the TME.

Implications: Leveraging a state-of-the-art organotypic tumor model, we demonstrated that CAFs-mediated HGF-MET signaling drive tumorigenic activities in TNBC and presents a therapeutic target.

Introduction

Breast tumors that lack expression of estrogen receptor (ER) and progesterone receptor (PR), and amplification of HER2 receptor are known as triple negative breast cancer (TNBC) (1). Although a few targeted therapies such as inhibitors of PARP or immune checkpoints are now available for advanced TNBC (2), cytotoxic chemotherapy remains the standard of care (3). Existing therapies for TNBC are largely ineffective due to drug resistance that eventually leads to relapse and metastasis within 3-5 years of diagnosis (4). Therefore, alternative treatment approaches are imperative to improve outcomes for TNBC patients. Recent evidence suggests that besides alterations in cancer cells, the tumor microenvironment (TME) and its interactions with cancer cells (i.e., tumor-stromal interactions) promote drug resistance and disease progression (5). Using the TME as a therapy target has gained momentum particularly for aggressive cancers such as TNBC that have a rich stroma and limited targeted therapies.

Cancer-associated fibroblasts (CAFs) are the most abundant stromal cells in the TME of TNBC (6). CAFs secrete paracrine signaling molecules that interact with cancer cells and promote tumor growth, drug resistance, and eventually metastasis (7). Recognizing the role of stroma-derived paracrine factors in tumorigenesis, several drugs are in clinical trials to target either CAFs, its secreted factors, or their corresponding receptors expressed on cancer cells (8). Despite progress in understanding the TME, identifying effective drugs against tumor-stromal interactions remains difficult (9). Typically, animal models and cell cultures are used for both mechanistic studies and testing drugs in preclinical stages. Animal models lack most, if not all, of human stroma and are incompatible with screening multiple compounds and dosing regimens needed in drug discovery (10). Monolayer cell cultures allow high throughput compound screening but lack the native architecture and components of tumor stroma and poorly predict drug responses in vivo. To address this technological gap, three-dimensional (3D) tumor models have been developed to recreate tumor-stromal interactions, including co-culture spheroids of cancer-stromal cells with or without ECM and microfluidic devices with tumor and stromal compartments (11-13). These models either do not recreate the spatial distribution of different components of the TME or are incompatible with automated

platforms for drug screening. Emerging organoid technologies partially address these shortcomings (14), with major caveats that include the long time needed to develop them and challenges to incorporate stromal cells.

We recently developed a 3D organotypic TNBC model that contains key components of the breast TME, i.e., a mass of cancer cells, activated fibroblasts, and ECM, and is compatible with automated liquid handling operations (15). Here, we leveraged this model and established that CAFs and TNBC cells predominantly communicate via HGF-MET paracrine signaling, activating several oncogenic pathways while promoting invasiveness and epithelial-to-mesenchymal transition (EMT) of TNBC cells. We also found that HGF-MET signaling was highly active in a lung stromal environment and promoted colony formation by TNBC cells. We identified drug combinations that significantly blocked stroma-mediated tumorigenic activities of TNBC cells.

Materials and Methods

Cell culture

MDA-MB-231, SUM159, Hs 578T, MDA-MB-157, HCC1806, and BT-20 TNBC cells and WI-38 lung fibroblast cells were purchased from ATCC. MDA-MB-231 and SUM159 TNBC cells were transduced to stably express GFP (16). Three different breast fibroblast cells were used: normal human mammary fibroblasts (HMF) stably transduced with mCherry protein (gift of Dr. Daniel Hayes, University of Michigan), CAFs derived from a human breast carcinoma tumor (CAF-1) and obtained from Neuromics (Cat. No. CAF06), and CAFs derived from an invasive ductal breast carcinoma tumor (CAF-2) and obtained from BioIVT (Cat. No. HPCCAFBR-05). CAFs were cultured as recommended by the vendors for up to five passages. MDA-MB-231, MDA-MB-157, Hs 578T, and HMF cells were cultured in Dulbecco's Modified Eagle Medium (DMEM, Sigma) supplemented with 10% fetal bovine serum (FBS, Sigma), 1% glutamine (Life Technologies), and 1% antibiotic (Life Technologies). HCC1806 cells were cultured in RPMI 1640 medium (Sigma) supplemented with 10% FBS and 1% antibiotic. SUM159 cells were cultured in Ham's F-12 medium (Gibco) supplemented with 10% FBS, 5 µg/ml insulin (Sigma), 2 µg/ml hydrocortisone (Sigma), 1% glutamine (Life Technologies), and 1% antibiotic. WI-

38 cells were cultured in Eagle's Minimum Essential Medium (EMEM, ATCC) supplemented with 10% FBS and 1% antibiotic. Cells were plated in T75 flasks (Thermo Fisher Scientific) and kept in a humidified incubator at 37°C and 5% CO_2. Cell lines were tested for mycoplasma contamination by PCR. After about 25 passages, the cells were replenished with fresh cultures from frozen stocks.

Human phospho-RTK array

A human phospho-RTK array (R&D Systems, Cat. No. ARY001B) was used to detect relative phosphorylation of 49 different RTKs on TNBC cells post-stimulation with conditioned media of CAF cells. TNBC cells (MDA-MB-231 and SUM159) were stimulated for 10 min with conditioned media from confluent cultures of CAFs (CAF-1 and CAF-2). For a negative control, TNBC cells were incubated with culture medium only for 10 min at 37°C. The cells were rinsed with cold PBS and lysed using lysis buffer 17 containing protease inhibitors (Aprotinin, Leupeptin, and Pepstatin). Protein concentrations were quantified using a BCA protein assay kit (Thermo Fisher Scientific). Each array was blocked for 1 h with array buffer 1 and incubated with 300 µg of protein lysate overnight at 4°C. The array was washed and incubated with HRP conjugated anti-phospho-tyrosine detection antibody and developed using FluorChem E imaging (ProteinSimple). The relative phosphorylation of each RTK in the blot array was quantified by measuring pixel densities of the corresponding pair of dots on the array in ImageJ and normalized with respect to its vehicle control.

Bead-based multiplex immunoassay

Conditioned media from confluent monolayer cultures of HMF, CAF-1, CAF-2, and WI-38 cells were collected from an overnight incubation. Concentrations of secreted soluble factors were quantified using a magnetic bead panel (Millipore Sigma, Cat. No. HAGP1MAG-12K) for HGF, FGF-1, FGF-2 and another panel (Millipore Sigma, Cat. No. HCYTA-60K) for EGF and PDGF-AB/BB. Briefly, each conditioned medium was centrifuged to remove debris. Then, the supernatant was incubated with the premixed antibody-immobilized beads overnight at 4°C on a titer plate shaker. The beads were

washed carefully three times with a wash buffer using a handheld magnet (Millipore, Cat. No. 40-285) to retain the magnetic beads in the well plate. Next, the beads were incubated with a detection antibody followed by addition of streptavidin-phycoerythrin. Median fluorescent intensity (MFI) from the beads was measured using a Luminex MAGPIX instrument. Standard curves were generated to determine concentrations of the soluble factors.

Organotypic tumor model and imaging of TNBC cell invasion

The organotypic tumor model was formed in two robotic micropatterning steps using an aqueous two-phase system (ATPS) technology with 5.0%(w/v) polyethylene glycol and 6.4%(w/v) dextran (17,18). First, 7.5×10^3 TNBC cells were microprinted in a nanodrop to form a spheroid in each well of a 384-well plate. Then, a drop containing 20 µl ice-cold rat tail type I collagen solution (Corning) and 1.5×10^4 suspended fibroblasts was dispensed into each well. The 384-well plate was incubated at 37°C for 30 min to form the tumor model with fibroblasts dispersed in a collagen gel containing a mass of TNBC cells. For confocal imaging, the tumor models were formed in a glass bottom 384-well plate (MatTek, Cat. No. PBK384G). Images were captured with a 10X objective on days 1 and 5 of culture (Nikon A1). TNBC cells without GFP were stained with Calcein AM (Thermo Fisher Scientific). Z-projected images were constructed from images of samples acquired with a z-spacing of 20 µm. NIS software was used for image acquisition and Fiji (ImageJ, NIH) was used for image analysis and 3D reconstruction. The total pixel area of TNBC cells when cultured with CAF-1 or CAF-2 was normalized to the pixel area of TNBC cells when cultured with HMF. Unlabeled collagen fibers were imaged using confocal reflectance microscopy.

Flow cytometry

To quantify the proliferation of TNBC cells in organotypic models 5 days after formation, the collagen matrix was digested using collagenase I (Sigma) and mechanical agitation for 15 min. Collagenase activity was neutralized by adding triple amounts of complete growth medium. The resulting suspension was centrifuged to obtain a cell pellet, which

was suspended in 300 µl of medium and then 50 µl of suspension of counting beads (CountBright, Invitrogen) was added. Cells were analyzed with a BD Accuri C6 flow cytometer. At least 10^3 counting bead events were acquired while running each sample. Non-fluorescing TNBC cells were used to remove the background fluorescence. The GFP^+ TNBC cells were gated from unstained fibroblasts. The absolute TNBC cell number was obtained as (number of TNBC events/number of bead events) × number of beads.

Quantitative PCR

Cells were harvested from organotypic cultures and lysed using a Total RNA Kit lysis buffer (Omega BioTek). The lysate was passed through homogenizer mini columns (Omega BioTek). Total RNA was obtained using an RNA isolation kit (Omega BioTek). After removing DNA using RNase-free DNase (Omega BioTek), purity and concentration of isolated RNA were assessed using optical density (OD) 260/280 spectrophotometry (Synergy H1M, BioTek Instruments). cDNA was synthesized from 1 µg of total RNA using random hexamer primers (Roche). Real-time qPCR was performed in a LightCycler 480 instrument II using a SYBR Green Master Mix (Roche). After combining 50 ng of cDNA with the primer and the SYBR Green Master Mix to a final volume of 15 µl, the reactions were incubated at 95°C for 5 min followed by 45 cycles of amplification, that is, at 95°C for 10 s, at 60°C for 10 s, and at 72°C for 10 s. The primer sequences for the genes are listed in Table S1. Gene expression values were calculated relative to β-actin and GAPDH using the ΔΔCt method. mRNA fold change was determined from the $2^{-\Delta\Delta Ct}$ method (19).

Western blotting

Organotypic cultures were treated with collagenase I for 15 min with added mechanical agitation. The collagenase activity was neutralized using triple amounts of complete growth media. The resulting suspension was centrifuged to obtain a cell pellet. The cells were washed with cold PBS and lysed with 500 µl of complete RIPA buffer containing 1% protease inhibitors and 1% phosphatase inhibitors. For stimulation experiments, MDA-MB-231 and SUM159 cells were stimulated for 10 min with CAF-1 and CAF-2 conditioned media with or without crizotinib (0.5 µM or 1 µM). For negative control, TNBC cells were

incubated with culture medium only for 10 min at 37°C. The cells were washed with cold PBS and harvested using RIPA buffer. The cell suspension was further sonicated twice at a 20% amplitude for 5 sec (Vibra-Cell, Sonics). A BCA protein quantification assay was used to measure total protein concentration from each sample, which was then loaded onto a 4-15% gel (Bio-rad) for electrophoresis. Each gel was transferred onto a nitrocellulose membrane by electroblotting, blocked in 5% non-fat dried milk prepared in wash buffer for 1 h, and incubated overnight with primary antibodies: phospho-p44/42 MAPK (Erk1/2, Cat. No. 9101), p44/42 MAPK (Erk1/2, Cat. No. 9102), phospho-Akt (Ser473, Cat. No. 4060), Akt (pan, Cat. No. 4691), phospho-Stat3 (Tyr705, Cat. No. 9145), Stat3 (Cat. No. 4904), E-Cadherin (Cat. No.14472), N-Cadherin (Cat. No. 13116), Vimentin (Cat. No. 5741), phospho-Met (Tr1234/1235, Cat. No. 3077), Met (Cat. No. 8198), and GAPDH (Cat. No. 5174), all purchased from Cell Signaling Technology. The membranes were washed and incubated with HRP-conjugated secondary antibody for 1 h. Detection was done using ECL chemiluminescence detection kit (GE Healthcare) with FluorChem E system.

Drug treatments of TNBC spheroids

Inhibitors of MAPK (trametinib, ulixertinib, SCH772984) and PI3K/Akt (dactolisib, apitolisib, VS-5584) were purchased from Selleckchem. Dactolisib was dissolved in dimethylformamide and all other compounds were dissolved in dimethyl sulfoxide. The compounds were used at 1×10^{-4} μM, 1×10^{-3} μM, 5×10^{-3} μM, 1×10^{-2} μM, 1×10^{-1} μM, 1×10^{0} μM, and 1×10^{1} μM against free floating spheroids of MDA-MB-231 and SUM159 cells. Untreated spheroids were kept in culture media. After 4 days of drug treatments, the GFP signal from TNBC cells was measured using a plate reader and the fluorescent signal was normalized to that from the vehicle control spheroids to construct dose−response curves (GraphPad Prism) and calculate LD_{50} values.

Cyclic treatment regimen

To model resistance of cancer cells to monotherapies (20), MDA-MB-231:CAF-1 co-culture spheroids at a 1:1 ratio were cyclically treated with 5 nM (i.e., $0.5\times LD_{50}$) trametinib

for 28 days. Each experiment included four cycles of treatment (T1, T2, T3, T4) each followed by a recovery phase (R1, R2, R3). Phase images were captured at the end of each cycle to approximate the volume of spheroids. The GFP signal from TNBC cells was normalized to that from day 0 to calculate a percent viability. A growth rate metric (k_c), defined as the difference in the volumes of spheroids after and before each treatment divided by 4 days treatment, was used to quantify trametinib resistance (20).

Combination treatments of organotypic cultures

Organotypic cultures were treated with crizotinib/trametinib or crizotinib/dactolisib combinations prepared in culture medium with 1% FBS. Each inhibitor was used at five concentrations, 0.1 – 50 nM for trametinib and dactolisib, and 1 – 5 μM for crizotinib, which were selected based on dose-responses of free-floating spheroids of the cells. Single-agent treatments with trametinib and dactolisib were also carried out, resulting in a 6×6 matrix of concentration pairs, each with four replicates. Treatments were renewed after 72 h. Confocal images of the cultures were captured on day 5. The area occupied by TNBC cells was measured, normalized with the respective vehicle control, and represented as an invasion area to quantify the effect of each treatment. The fraction of cells affected by each treatment was calculated as 1-invasion area. A synergy analysis was performed to generate a combination index (CI) for pairs of drugs (21).

Colony formation assay and immunofluorescence imaging of proliferative cells

TNBC cells (MDA-MB-231, MDA-MB-157, SUM159, Hs 578T), with or without WI-38 lung fibroblast cells, were seeded as a single cell suspension in a 1.2% (w/v) methylcellulose (Sigma) gel made using 1% FBS-containing medium. A 1:4 ratio of TNBC:WI-38 cells was used and each well of a 384-well plate contained 50 TNBC cells and 200 WI-38 cells. Culture medium with 1% FBS was replaced every 3 days. The cultures were treated with 0.5 μM crizotinib and maintained for 8-10 days to image the colonies. The TNBC cells without GFP were stained with Calcein AM prior to imaging at a 2.5X magnification. An in-house python code in ImageJ was used to automatically detect the colonies in each image and compute their areas. A threshold colony diameter

of 75 μm was used for statistical analysis. The TNBC colonies were fixed using 4% paraformaldehyde (PFA) in PBS for 15 min at room temperature, washed with PBS for 10 min, and blocked with 3% donkey serum for 1 h at room temperature. Cells were permeabilized using 0.3% Triton X-100 in PBS. Samples were incubated overnight with a Ki-67 rabbit antibody in 1% BSA and 0.3% Triton X-100 in PBS (Cell Signaling, Cat. No. 9027). Samples were washed and incubated with a rhodamine red donkey anti-rabbit IgG (Jackson ImmunoResearch, 1:100, Cat. No. 711-295-152) for 1h and imaged. Ki-67$^+$ cells were counted per TNBC colony and Ki-67/colony area ratios were normalized to the average in the respective vehicle control group, i.e., TNBC cells without WI-38 cells and crizotinib treatment.

Bioinformatics analysis of data from breast cancer patients

The mRNA expression data from 2509 publicly available cases of invasive breast carcinoma were downloaded from The Cancer Genome Atlas (TCGA, METABRIC dataset) (22), using cBioPortal (http://www.cbioportal.org/). A query was performed to analyze co-expression of EGFR and MET genes. Co-expression of EGFR and MET proteins was also analyzed using protein expression data from the Firehose legacy breast cancer dataset (TCGA). The activities of p-EGFR and p-MET were determined from The Cancer Proteome Atlas (TCPA) available through MD Anderson Cancer Center (23).

Gene set enrichment analysis (GSEA)

Gene expression data of GSE138139 was downloaded from the GEO database. For GSEA, the number of permutations was set to 1,000. The platform of this dataset is the GPL1261 Affymetrix mouse genome 430 2.0 array. The enrichment score was calculated according to metastasis status (lung metastasis versus parental breast cancer cells). Differences of a nominal $p<0.05$ and an FDR less than 25% defined significance.

Statistical analysis

Data were first checked for normality using the Anderson-Darling method in MINITAB. For normally-distributed data, one-way ANOVA with Tukey's pairwise comparisons was

used to compare means among three or more samples. A two-tailed, unpaired t-test was used to compare two experimental groups. Normally-distributed data from experiments were expressed as mean ± standard error. Non-Gaussian distributed data were analyzed using two-tailed Mann-Whitney test. Values of $p<0.05$ denoted statistical significance.

Data availability

The data generated in this study are available within the article and its Supplementary Data file. Any materials may be made available from the corresponding author upon request.

Results

CAFs interact with TNBC cells via HGF-MET pathway

We stimulated TNBC cells with conditioned medium of CAF-1 and CAF-2 cultures and used a phospho-RTK array to detect activities of 49 RTKs in MDA-MB-231 and SUM159 TNBC cells (Fig. 1a and Fig. S1) (24). While both TNBC cells had high basal EGFR activity, stimulation with CAFs significantly activated MET. CAF-1 led to 25 and 30-fold increase in pMET levels and marginally affected pEGFR by 0.7 and 1.5-fold in MDA-MB-231 and SUM159 cells, respectively (Fig. 1b). CAF-2 also increased pMET by 3.7 and 5.5-fold and minimally changed pEGFR by 0.8 and 1.3-fold in MDA-MB-231 and SUM159 cells, respectively. Thus, CAFs predominantly activated MET in TNBC cells. To further validate this finding, we treated six different TNBC cells with conditioned media from the CAFs and found significant activation of MET in all six TNBC cells by CAF-1 and in five of the TNBC cells by CAF-2 (Fig. 1c-d). Despite MET protein expression in the TNBC cells (i.e., high t-MET levels), paracrine signaling with CAFs activated it (i.e., p-MET) (Fig. 1c). We ensured that MET activation was indeed due to paracrine signaling with CAFs using an immunoassay that showed both CAFs secrete high levels of the MET ligand, HGF, i.e., ~10.2 ng/ml by CAF-1 and ~1 ng/ml by CAF-2 (Fig. 1e). In contrast, HMFs secreted only 50 pg/ml of HGF. Other soluble factors such as EGF, FGF-1 and FGF-2, and PDGF AA/AB were not detectable. Taken together, these results indicate that CAFs from patients secrete HGF and predominantly activate MET in TNBC cells.

CAFs activate multiple oncogenic pathways in TNBC cells

Active RTKs regulate various signaling pathways that drive breast cancer progression (25). We evaluated activities of several prominent pathways in breast cancers including MAPK, PI3K/Akt, and JAK/STAT. While MDA-MB-231 cells had basal MAPK/ERK activity due to an activating mutation in K-Ras (26), CAF-1 led to activation of both Akt and STAT3, whereas CAF-2 only activated Akt (Fig. 2a). In SUM159 cells that had basal PI3K/Akt pathway activity due to a mutation in PI3K (26), both CAFs activated ERK and STAT3 signaling (Fig. 2a). CAF-1 had a greater effect in activation of these pathways than CAF-2 because of its higher HGF production that led to significantly higher MET activation in TNBC cells (Fig. 1c-d). To validate the role of HGF-MET signaling in activating these pathways, we used a MET inhibitor, crizotinib, against TNBC cells stimulated with CAF-1. We selected only CAF-1 for this experiment because of its greater effect on promoting oncogenic signaling in TNBC cells. This treatment led to a dose-dependent significant reduction in activation of ERK, Akt, and STAT3 in both MDA-MB-231 and SUM159 cells (Fig. 2b). Overall, these results established that CAFs promote several downstream pathways in TNBC cells through HGF-MET signaling.

MET expression and activity in patient tumors

To determine the clinical relevance of MET in TNBC, we analyzed MET gene expression in different breast cancer subtypes in TCGA. Basal and claudin-low subtypes of breast cancer, which primarily represent TNBC, showed significantly higher expression of MET than other subtypes (Fig. 3a). We also found a moderate, but significant correlation between MET and EGFR at both gene and protein levels (Fig. 3b). To determine functional activities of MET and EGFR in breast tumors, we analyzed data for invasive breast carcinomas and found a significant correlation between p-MET and p-EGFR (Fig. 3c). This analysis of data from patient tumors underlines the significance of MET activity in TNBC, and together with our results, suggests a critical role for CAFs to predominantly activate MET in $EGFR^+$ TNBC cells.

CAFs promote pro-metastatic functions in TNBC cells

Our organotypic tumor 3D model mimics the architecture and positioning of cancer and stromal cells in solid tumors. The model has a matrix stiffness of ~2.5 kPa as in human breast tumors (Fig. 4a) (15,27). Using this model, we studied the role of CAFs on matrix invasion of TNBC cells. We found that unlike HMF cells, CAF-1 and CAF-2 promoted ECM invasion of MDA-MB-231 and SUM159 cells by up to ~2.5-fold (Fig. 4b-c). Furthermore, our analysis of organotypic models showed that both CAFs promoted proliferation of the TNBC cells by up to ~1.3-fold within 5 days (Fig. 4d-e).

Due to the role of EMT in local invasion of cancer cells and metastasis (28), we investigated whether CAFs promote an EMT phenotype in TNBC cells. Invading TNBC cells in organotypic models containing CAF-1 or CAF-2 displayed a significantly more elongated morphology compared to those with HMF cells (Fig. 5a). To validate this result, we quantified gene expression of several EMT transcription factors. Co-cultures with CAF-1 and CAF-2 upregulated most EMT markers in TNBC cells (Fig. 5b). CAF-1 enhanced expression of SLUG and FOXC2 in MDA-MB-231 cells and SNAIL and ZEB2 in SUM159 cells by more than 3-fold. CAF-2 also increased expression of SLUG and FOXC2 by nearly or more than 2-fold in MDA-MB-231 cells and SNAIL in SUM159 cells by over 2-fold. We further validated these results and showed that stimulation with CAF-1 conditioned medium led to elevation of vimentin in MDA-MB-231 cells and N-cadherin in SUM159 cells (Fig. 5c). CAF-2 cells did not induce a detectable change in these proteins in the TNBC cells. Overall, these results indicate that CAFs shift these mesenchymal-like TNBC cells further toward a mesenchymal phenotype.

Modeling resistance of TNBC cells to single-agent treatments

Frequent emergence of drug resistance to monotherapies in solid tumors typically necessitates combination therapies to increase treatment efficacy and durability (29). Next, we asked to what extent single-agent targeting of constitutively-active oncogenic pathways in TNBC cells would lead to drug resistance and a potential function of HGF-cMET signaling in drug resistance. To select drug compounds for these experiments, we used TNBC spheroids and performed a dose-dependent screening of a set of molecular

inhibitors against MAPK and PI3K/Akt pathways (Fig. S2). Our quantitative analysis showed that the most effective inhibitors were trametinib against MDA-MB-231 cells with an LD_{50} of 10 nM and dactolisib against SUM159 cells with an LD_{50} of 1 μM. Then, we treated MDA-MB-231:CAF-1 co-culture spheroids with trametinib in a cyclic regimen to mimic intermittent chemotherapy cycles (Fig. 6a). Trametinib reduced the size of spheroids during the first two treatment rounds (T1 and T2) (Fig. 6b) and reduced cancer cell viability to 41% at the end of T2 (Fig. 6c). However, after the second recovery round (R2), trametinib became significantly less effective. At the end of the 28-day regimen, spheroids treated with trametinib were 3.04-fold larger than those after T1 and the GFP fluorescence intensity of the MDA-MB-231 cells, i.e., an approximate measure of number of cells, increased by 3.11-fold compared to that after T1. We used a growth rate metric (k_c) to quantify the treatment effect (Fig. 6d). Although k_c for the spheroids reduced during T1 and T2, it significantly increased during T3 and T4. The k_c values of spheroids from T1 to T4 increased from -0.0059 mm^3/day to 0.0172 mm^3/day. To elucidate the underlying mechanisms, we evaluated activation of ERK, Akt, and MET following T1 and T3 treatments (Fig. 6e). Trametinib treatment reduced pERK and pMET levels but upregulated pAKT during T1. Following T3, there was significant activation of ERK and MET and persistent activity of Akt. These findings suggest feedback signaling between PI3K/Akt and MAPK/MEK pathways and gain of MET activity to drive ERK signaling as potential mechanisms of trametinib resistance of TNBC cells.

Combination treatments to suppress tumorigenic activities of TNBC cells

Next, we evaluated the feasibility of a combination treatment strategy to simultaneously suppress proliferation, invasion, and EMT of TNBC cells in organotypic cultures. Because HGF from CAFs activated MET in TNBC cells, we hypothesized that treatments blocking the HGF-MET axis and its downstream pathways could potentially inhibit tumorigenic activities of TNBC cells. To test this hypothesis, we selected a combination of inhibitors of MET and MAPK pathway for MDA-MB-231 cells and MET and PI3K/Akt pathway for SUM159 cells and performed matrix-style combination treatments. This selection reflects different constitutively active kinase pathways in the TNBC cells, i.e., MAPK pathway in

MDA-MB-231 and PI3K/Akt pathway in SUM159 cells (Fig. 2a). We used CAF-1 for these experiments because it had a greater effect on promoting invasion, proliferation, EMT, and oncogenic signaling in TNBC cells than CAF-2.

Representative images of MDA-MB-231 and SUM159 cells in organotypic cultures under single-agent and combination treatments and the quantified inhibition of invasion are shown in Fig. 7a-d. While each compound alone reduced cancer cell invasion, the combination treatments more effectively inhibited invasion at low concentrations. With the organotypic cultures of MDA-MB-231, trametinib/crizotinib up to and including the 5 nM/1 μM pair showed significantly greater effects than the individual drugs. The 5 nM/1 μM pair synergistically reduced cell invasion by 93% and resulted in CI=0.34. With the organotypic cultures of SUM159, crizotinib/dactolisib up to and including the 1 μM/1 μM pair were more effective than each compound alone with the combination blocking SUM159 cell invasion by up to 96% with a CI = 0.39. Although the drug combinations also reduced MDA-MB-231 and SUM159 cell proliferation in organotypic models by 1.76-fold and 2.0-fold (Fig 7e-f), respectively, results suggest that TNBC proliferation was primarily driven by the constitutive pathway in each TNBC cell line because reduction in proliferation was mainly realized using the respective inhibitor of each pathway rather than crizotinib.

Next, we studied inhibitory effects of the treatments on downstream signaling pathways. The crizotinib/trametinib pair downregulated activities of MAPK, PI3K/Akt, and JAK/STAT pathways in MDA-MB-231 cells, significantly greater than those from the respective responses when each compound was used alone (Fig. 7g). Additionally, it significantly reduced expression of various EMT gene and protein markers (Fig. 7h-i). With SUM159 organotypic cultures, the dactolisib/crizotinib pair also significantly reduced activities of the three signaling pathways (Fig. 7j) and EMT markers (Fig. 7k-l). Overall, these results provide compelling evidence that the selected combinations treatments effectively block CAFs-mediated pro-metastatic activities of TNBC cells by simultaneously blocking signaling activities in multiple prominent oncogenic pathways.

HGF-MET pathway promotes TNBC survival and colony formation in lung stroma

Due to the prevalence of TNBC metastasis to lung, we asked whether HGF-MET pathway has a role in supporting TNBC cell survival and colony formation in the lung. We used a Molecular Signatures Database (MSigDB) hallmark gene set collection and derived 14 MET signature genes based on their association with activated MET (30). Our analysis of results from a study of a murine metastasis model of human TNBC showed that these genes were significantly enriched in lung metastasis (Fig. S3a) (31). This was consistent with other studies that showed lung stromal cells secrete high levels of HGF. To investigate functional effects of HGF-MET signaling in lung stroma, we used WI-38 lung fibroblast cells to determine to what extent they impact colony formation of TNBC cells. First, we validated that WI-38 cells activate MET receptors in both MDA-MB-231 and SUM159 TNBC cells (Fig. S3b). We ensured the specificity of this activity by analyzing the secretome of WI-38 cells and found that these cells secrete ~7.2 ng/ml of HGF (Fig. S3c).

To study the role of lung fibroblasts in survival and proliferation of TNBC cells, we developed a 3D lung stromal environment consisting of a methylcellulose hydrogel and dispersed WI-38 cells. The hydrogel also contained single TNBC cells to represent metastatic cells. We used four different TNBC cell lines at a 1:4 ratio to WI-38 cells to mimic the relatively small population of cancer cells compared to the resident stromal cells in metastatic sites. Results showed that WI-38 cells significantly promote colony formation of SUM159, Hs578T, and MDA-MB-157 cells by 1.61, 4.0, and 3.0-fold, respectively (Fig. S3d). We validated that this response was indeed due to the HGF-MET pathway by showing that crizotinib significantly reduced colony formation of all three TNBC cells (Fig. S3d). Immunofluorescent staining of the cultures also showed a significant increase in Ki-67^{+} TNBC cells, which was reversed by blocking the HGF-MET axis (Fig. S3e). We note that WI-38 cells did not increase colony formation of MDA-MB-231 cells, consistent with a study that showed formation of MDA-MB-231 lung micrometastases significantly larger than our selected threshold to quantify colonies requires a much longer time than we used (32). Collectively, these results demonstrate

that lung fibroblasts provide a permissive niche for survival and metastatic colonization of TNBC cells via the HGF-MET axis and suggest that blocking this pathway may provide benefits against both primary TNBC and lung metastasis.

Discussion

TNBC is a heterogeneous disease that presents six different subtypes with significant activities of RTKs and downstream Ras/Raf/MEK/ERK and PI3K/Akt/mTOR pathways (33,34). Although PARP and immune checkpoint inhibitors are now available for advanced TNBC (2), cytotoxic chemotherapy remains the mainstay treatment. Thus, disrupting tumor-stromal interactions may provide new targeted therapies for TNBC. We developed an organotypic tumor model to mechanistically study interactions of TNBC cells with patient-derived CAFs. Patient-derived CAFs predominantly secreted HGF, consistent with studies that showed CAFs in breast tumors produce as high as 50 ng/ml of HGF (35). However, CAFs from different patients showed a significant difference in HGF production due to inter-tumoral heterogeneity that is a characteristic of CAFs in breast tumors (Fig. S4) (36,37). Although several reports have shown that breast cancer cells can produce HGF to activate MET in an autocrine signaling manner (38), we did not detect HGF in supernatants of TNBC cells. Furthermore, all six TNBC cell lines used had endogenous MET expression, in agreement with data from human breast tumors showing significantly higher MET gene expression in basal and claudin-low subtypes compared to other breast cancers (Fig. 3). Other studies have shown that MET is frequently overexpressed in malignant breast tissues and TNBC tumors (39,40), and its expression is a strong independent marker for poor prognosis in breast carcinoma (41,42). Consistent with the role of stroma in breast tumorigenicity (35,43), CAFs from patients significantly promoted proliferation, matrix invasion, and EMT of TNBC cells in our organotypic tumor model. Our analysis of RTK activities of TNBC cells showed high basal activation of EGFR, consistent with EGFR overexpression in up to 78% of TNBC tumors (40,44). But in the presence of CAFs, the HGF-MET axis was the dominant oncogenic signaling pathway. This finding highlights a potential reason for the failure of anti-EGFR monotherapies in TNBC (45), consistent with our results that showed EGFR inhibitors

were not effective against TNBC cell invasiveness (Fig. S5a) or CAFs-mediated MET activation (Fig. S5b). However, crizotinib alone significantly reduced matrix invasion and EGFR activity of TNBC cells (Fig. S5a). These results emphasize limitations of targeting only genetic aberrations of cancer cells and the importance of tumor-stromal interactions as a therapeutic target in TNBC. Using a defined matrix in our model is a major advantage to capture effects of specific CAFs-TNBC signaling without additional stimulatory and inhibitory factors present in animal-derived matrices such as Matrigel. Selecting human collagen for our model was guided by previous finding that TNBC has a significant enrichment for collagen deposition compared with the luminal subtypes (46).

Leveraging our 3D organotypic model that allows mechanistic studies to guide treatments, we investigated both single-agent and combination treatments against HGF-MET and its downstream pathways. As expected, single-agent inhibition of the MAPK pathway in a long-term, cyclic treatment regimen led to resistance of TNBC cells. Consistent with our finding, prior studies have shown feedback activation of oncogenic kinase pathways as a major resistance mechanism (20,21). To simultaneously suppress matrix invasion, proliferation, and EMT of TNBC cells, we designed combination treatments against both TNBC-CAFs interactions and basal active signaling in TNBC cells, i.e., crizotinib/trametinib for MDA-MB-231 cells and crizotinib/dactolisib for SUM159 cells. This strategy was critical because targeting only the TNBC-CAFs interaction or the TNBC cells proved insufficient. For example, using a MAPK inhibitor (trametinib) alone against MDA-MB-231 cells led to drug resistance (Fig. 6), whereas targeting only the CAFs-mediated MET activation using crizotinib alone reduced but did not block activities of signaling proteins in TNBC cells (Fig. 7). We note that crizotinib alone was very effective in downregulating oncogenic pathways in TNBC cells with a brief 10 min treatment, but this was reversed over a 5-day treatment, indicating that TNBC cells become resistant to monotherapy with crizotinib as well. The combination treatment successfully blocked activities of these pathways. In addition to the role of HGF-MET in primary tumor progression, this signaling promoted colony forming capability of TNBC cells in a lung stromal environment, consistent with the role of lung stromal cells in

promoting metastatic colonization of cancer cells (32,47). Other studies showed that HGF significantly increased lung metastasis of breast cancer cells in mouse models (48,49). Interestingly, disrupting HGF-MET using crizotinib significantly reduced colony formation of TNBC cells in our model of lung stroma, suggesting that this pathway has therapeutic value against TNBC metastases formation in the lungs.

In conclusion, we developed an organotypic 3D tumor model and demonstrated that interactions between TNBC cells and patient-derived CAFs occur predominantly through HGF-MET axis. This tumor-stromal signaling activated several oncogenic pathways and promoted pro-metastatic activities of TNBC cells and colony formation in the lung stroma. We developed a design-driven approach and showed the feasibility of targeting tumor-stromal interactions using specific drug combinations to significantly inhibit matrix invasion, proliferation, and EMT of TNBC cells in a primary tumor environment and their metastatic colonization in a lung stromal environment. Our engineered tumor model is conducive to phenotypic and mechanistic studies to identify new therapeutic opportunities against tumor-stromal interactions and develop and screen the effectiveness of various treatment combinations and regimens. We also note that CAFs also degrade and deposit ECM and change its mechanical properties. Investigating integrated effects of biochemical and mechanical inputs to facilitate cancer cell invasiveness can inform targeting of tumor-stromal interactions.

Acknowledgements: This research was supported by NIH/NCI grants CA225549 and CA216413 (H. Tavana) and NSF grant 1801591 (H. Tavana).

References

1. Rakha EA, El-Sayed ME, Green AR, Lee AHS, Robertson JF, Ellis IO. Prognostic markers in triple-negative breast cancer. Cancer-Am Cancer Soc **2007**;109(1):25-32 doi 10.1002/cncr.22381.
2. Lyons TG. Targeted Therapies for Triple-Negative Breast Cancer. Curr Treat Option On **2019**;20(11) doi 10.1007/s11864-019-0682-x.
3. Hutchinson KE, Yost SE, Chang CW, Johnson RM, Carr AR, McAdam PR*, et al.* Comprehensive Profiling of Poor-Risk Paired Primary and Recurrent Triple-Negative Breast Cancers Reveals Immune Phenotype Shifts. Clin Cancer Res **2020**;26(3):657-68 doi 10.1158/1078-0432.Ccr-19-1773.
4. van Roozendaal LM, Smit LHM, Duijsens GHNM, de Vries B, Siesling S, Lobbes MBI*, et al.* Risk of regional recurrence in triple-negative breast cancer patients: a Dutch cohort study. Breast Cancer Res Tr **2016**;156(3):465-72 doi 10.1007/s10549-016-3757-4.
5. Junttila MR, de Sauvage FJ. Influence of tumour micro-environment heterogeneity on therapeutic response. Nature **2013**;501(7467):346-54 doi 10.1038/nature12626.
6. Kalluri R. The biology and function of fibroblasts in cancer. Nat Rev Cancer **2016**;16(9):582-98 doi 10.1038/nrc.2016.73.
7. Straussman R, Morikawa T, Shee K, Barzily-Rokni M, Qian ZR, Du JY*, et al.* Tumour micro-environment elicits innate resistance to RAF inhibitors through HGF secretion. Nature **2012**;487(7408):500-U118 doi 10.1038/nature11183.
8. Sahai E, Astsaturov I, Cukierman E, DeNardo DG, Egeblad M, Evans RM*, et al.* A framework for advancing our understanding of cancer-associated fibroblasts. Nat Rev Cancer **2020**;20(3):174-86 doi 10.1038/s41568-019-0238-1.
9. Jin MZ, Jin WL. The updated landscape of tumor microenvironment and drug repurposing. Signal Transduct Tar **2020**;5(1) doi 10.1038/s41392-020-00280-x.
10. Singh M, Ferrara N. Modeling and predicting clinical efficacy for drugs targeting the tumor milieu. Nat Biotechnol **2012**;30(7):648-57 doi 10.1038/nbt.2286.

11. Ham SL, Thakuri PS, Plaster M, Li J, Luker KE, Luker GD*, et al.* Three-dimensional tumor model mimics stromal - breast cancer cells signaling. Oncotarget **2018**;9(1):249-67 doi 10.18632/oncotarget.22922.
12. Truong DD, Kratz A, Park JG, Barrientos ES, Saini H, Nguyen T*, et al.* A Human Organotypic Microfluidic Tumor Model Permits Investigation of the Interplay between Patient-Derived Fibroblasts and Breast Cancer Cells. Cancer Res **2019**;79(12):3139-51 doi 10.1158/0008-5472.Can-18-2293.
13. Singh S, Tran S, Putman J, Tavana H. Three-dimensional models of breast cancer-fibroblasts interactions. Exp Biol Med **2020**;245(10):879-88 doi 10.1177/1535370220917366.
14. Sachs N, de Ligt J, Kopper O, Gogola E, Bounova G, Weeber F*, et al.* A Living Biobank of Breast Cancer Organoids Captures Disease Heterogeneity. Cell **2018**;172(1-2):373 doi 10.1016/j.cell.2017.11.010.
15. Singh S, Ray LA, Thakuri PS, Tran S, Konopka MC, Luker GD*, et al.* Organotypic breast tumor model elucidates dynamic remodeling of tumor microenvironment. Biomaterials **2020**;238 doi 10.1016/j.biomaterials.2020.119853.
16. Song JW, Cavnar SP, Walker AC, Luker KE, Gupta M, Tung YC*, et al.* Microfluidic Endothelium for Studying the Intravascular Adhesion of Metastatic Breast Cancer Cells. Plos One **2009**;4(6) doi 10.1371/journal.pone.0005756.
17. Atefi E, Lemmo S, Fyffe D, Luker GD, Tavana H. High Throughput, Polymeric Aqueous Two-Phase Printing of Tumor Spheroids. Adv Funct Mater **2014**;24(41):6509-15 doi 10.1002/adfm.201401302.
18. Tavana H, Jovic A, Mosadegh B, Lee QY, Liu X, Luker KE*, et al.* Nanolitre liquid patterning in aqueous environments for spatially defined reagent delivery to mammalian cells. Nat Mater **2009**;8(9):736-41 doi 10.1038/Nmat2515.
19. Joshi R, Thakuri PS, Buchanan JC, Li J, Tavana H. Microprinted Stem Cell Niches Reveal Compounding Effect of Colony Size on Stromal Cells-Mediated Neural Differentiation. Adv Healthc Mater **2018**;7(5) doi 10.1002/adhm.201700832.

20. Thakuri PS, Luke GD, Tavana H. Cyclical Treatment of Colorectal Tumor Spheroids Induces Resistance to MEK Inhibitors. Transl Oncol **2019**;12(3):404-16 doi 10.1016/j.tranon.2018.11.009.
21. Thakuri PS, Gupta M, Joshi R, Singh S, Tavana H. Synergistic Inhibition of Kinase Pathways Overcomes Resistance of Colorectal Cancer Spheroids to Cyclic Targeted Therapies. Acs Pharmacol Transl **2019**;2(4):275-84 doi 10.1021/acsptsci.9b00042.
22. Pereira B, Chin SF, Rueda OM, Vollan HKM, Provenzano E, Bardwell HA*, et al.* The somatic mutation profiles of 2,433 breast cancers refine their genomic and transcriptomic landscapes (vol 7, 11479, 2016). Nat Commun **2016**;7 doi 10.1038/ncomms11908.
23. Li J, Lu YL, Akbani R, Ju ZL, Roebuck PL, Liu WB*, et al.* TCPA: a resource for cancer functional proteomics data. Nat Methods **2013**;10(11):1046-7 doi 10.1038/Nmeth.2650.
24. Thakuri PS, Gupta M, Singh S, Joshi R, Glasgow E, Lekan A*, et al.* Phytochemicals inhibit migration of triple negative breast cancer cells by targeting kinase signaling. Bmc Cancer **2020**;20(1) doi 10.1186/s12885-019-6479-2.
25. Spangle JM, Roberts TM. Epigenetic regulation of RTK signaling. J Mol Med **2017**;95(8):791-8 doi 10.1007/s00109-017-1546-0.
26. Hollestelle A, Elstrodt F, Nagel JHA, Kallemeijn WW, Schutte M. Phosphatidylinositol-3-OH kinase or RAS pathway mutations in human breast cancer cell lines. Mol Cancer Res **2007**;5(2):195-201 doi 10.1158/1541-7786.Mcr-06-0263.
27. Plodinec M, Loparic M, Monnier CA, Obermann EC, Zanetti-Dallenbach R, Oertle P*, et al.* The nanomechanical signature of breast cancer. Nat Nanotechnol **2012**;7(11):757-65 doi 10.1038/Nnano.2012.167.
28. Bakir B, Chiarella AM, Pitarresi JR, Rustgi AK. EMT, MET, Plasticity, and Tumor Metastasis. Trends Cell Biol **2020**;30(10):764-76 doi 10.1016/j.tcb.2020.07.003.

29. Tolcher AW, Peng W, Calvo E. Rational Approaches for Combination Therapy Strategies Targeting the MAP Kinase Pathway in Solid Tumors. Mol Cancer Ther **2018**;17(1):3-16 doi 10.1158/1535-7163.Mct-17-0349.
30. Liberzon A, Birger C, Thorvaldsdottir H, Ghandi M, Mesirov JP, Tamayo P. The Molecular Signatures Database Hallmark Gene Set Collection. Cell Syst **2015**;1(6):417-25 doi 10.1016/j.cels.2015.12.004.
31. Kanaji N, Yokohira M, Nakano-Narusawa Y, Watanabe N, Imaida K, Kadowaki N*, et al.* Hepatocyte growth factor produced in lung fibroblasts enhances non-small cell lung cancer cell survival and tumor progression. Resp Res **2017**;18 doi 10.1186/s12931-017-0604-z.
32. Pein M, Insua-Rodriguez J, Hongu T, Riedel A, Meier J, Wiedmann L*, et al.* Metastasis-initiating cells induce and exploit a fibroblast niche to fuel malignant colonization of the lungs. Nat Commun **2020**;11(1) doi 10.1038/s41467-020-15188-x.
33. Lawrence RT, Perez EM, Hernandez D, Miller CP, Haas KM, Irie HY*, et al.* The Proteomic Landscape of Triple-Negative Breast Cancer. Cell Rep **2015**;11(4):630-44 doi 10.1016/j.celrep.2015.03.050.
34. Lehmann BD, Bauer JA, Chen X, Sanders ME, Chakravarthy AB, Shyr Y*, et al.* Identification of human triple-negative breast cancer subtypes and preclinical models for selection of targeted therapies. J Clin Invest **2011**;121(7):2750-67 doi 10.1172/Jci45014.
35. Tyan SW, Kuo WH, Huang CK, Pan CC, Shew JY, Chang KJ*, et al.* Breast Cancer Cells Induce Cancer-Associated Fibroblasts to Secrete Hepatocyte Growth Factor to Enhance Breast Tumorigenesis. Plos One **2011**;6(1) doi 10.1371/journal.pone.0015313.
36. Kieffer Y, Hocine HR, Gentric G, Pelon F, Bernard C, Bourachot B*, et al.* Single-Cell Analysis Reveals Fibroblast Clusters Linked to Immunotherapy Resistance in Cancer. Cancer Discov **2020**;10(9):1330-51 doi 10.1158/2159-8290.Cd-19-1384.

37. Pelon F, Bourachot B, Kieffer Y, Magagna I, Mermet-Meillon F, Bonnet I*, et al.* Cancer-associated fibroblast heterogeneity in axillary lymph nodes drives metastases in breast cancer through complementary mechanisms. Nat Commun **2020**;11(1) doi 10.1038/s41467-019-14134-w.
38. Tuck AB, Park M, Sterns EE, Boag A, Elliott BE. Coexpression of hepatocyte growth factor and receptor (Met) in human breast carcinoma. Am J Pathol **1996**;148(1):225-32.
39. Graveel CR, DeGroot JD, Su YL, Koeman J, Dykema K, Leung S*, et al.* Met induces diverse mammary carcinomas in mice and is associated with human basal breast cancer. P Natl Acad Sci USA **2009**;106(31):12909-14 doi 10.1073/pnas.0810403106.
40. Jin L, Fuchs A, Schnitt SJ, Yao Y, Joseph A, Lamszus K*, et al.* Expression of scatter factor and c-met receptor in benign and malignant breast tissue. Cancer-Am Cancer Soc **1997**;79(4):749-60 doi Doi 10.1002/(Sici)1097-0142(19970215)79:4<749::Aid-Cncr12>3.0.Co;2-#.
41. Ghoussoub RAD, Dillon DA, D'Aquila T, Rimm EB, Fearon ER, Rimm DL. Expression of c-met is a strong independent prognostic factor in breast carcinoma. Cancer-Am Cancer Soc **1998**;82(8):1513-20 doi 10.1002/(Sici)1097-0142(19980415)82:8<1513::Aid-Cncr13>3.0.Co;2-7.
42. Ponzo MG, Lesurf R, Petkiewicz S, O'Malley FP, Pinnaduwage D, Andrulis IL*, et al.* Met induces mammary tumors with diverse histologies and is associated with poor outcome and human basal breast cancer. P Natl Acad Sci USA **2009**;106(31):12903-8 doi 10.1073/pnas.0810402106.
43. Soon PS, Kim E, Benn DE, Baxter R. Chemokines released by breast cancer-associated fibroblasts induce epithelial to mesenchymal transition in MCF7 breast cancer cells. Cancer Res **2015**;75 doi 10.1158/1538-7445.Sabcs14-P4-04-27.
44. Martin V, Botta F, Zanellato E, Molinari F, Crippa S, Mazzucchelli L*, et al.* Molecular characterization of EGFR and EGFR-downstream pathways in triple

negative breast carcinomas with basal like features. Histol Histopathol **2012**;27(6):785-92.

45. Ali R, Wendt MK. The paradoxical functions of EGFR during breast cancer progression. Signal Transduct Tar **2017**;2 doi 10.1038/sigtrans.2016.42.
46. Acerbi I, Cassereau L, Dean I, Shi Q, Au A, Park C*, et al.* Human breast cancer invasion and aggression correlates with ECM stiffening and immune cell infiltration. Integr Biol-Uk **2015**;7(10):1120-34 doi 10.1039/c5ib00040h.
47. Martin YD, Park D, Ramachandran A, Ombrato L, Calvo F, Chakravarty P*, et al.* Mesenchymal Cancer Cell-Stroma Crosstalk Promotes Niche Activation, Epithelial Reversion, and Metastatic Colonization. Cell Rep **2015**;13(11):2456-69 doi 10.1016/j.celrep.2015.11.025.
48. Gallego MI, Bierie B, Hennighausen L. Targeted expression of HGF/SF in mouse mammary epithelium leads to metastatic adenosquamous carcinomas through the activation of multiple signal transduction pathways. Oncogene **2003**;22(52):8498-508 doi 10.1038/sj.onc.1207063.
49. Lee WJ, Chen WK, Wang CJ, Lin WL, Tseng TH. Apigenin inhibits HGF-promoted invasive growth and metastasis involving blocking PI3K/Akt pathway and beta 4 integrin function in MDA-MB-231 breast cancer cells. Toxicol Appl Pharm **2008**;226(2):178-91 doi 10.1016/j.taap.2007.09.013.

Figure Legends

Figure 1. CAFs interact with TNBC cells predominantly through the HGF-MET pathway. **(a)** Phospho-RTK arrays of MDA-MB-231 and SUM159 monoculture cells stimulated with CAF-1 and CAF-2. Colored boxes in the arrays represent pEGFR (blue) and pMET (brown and purple). **(b)** Pixel densities representing activities of EGFR and MET from the treatments normalized with the respective vehicle control and represented as an activity fold change. Error bars represent standard errors from a mean value. Data represent three separate experiments. **(c)** MET activation in six different TNBC cell lines due to stimulation with CAF-1 and CAF-2. **(d)** Quantified levels of p-MET/t-MET in TNBC cells stimulated with CAF-1 and CAF-2 and statistically compared with a vehicle control group for each cell line. Data represent two separate experiments with two replicates. *p<0.05 was calculated using two-tailed, unpaired t-tests. **(e)** HGF levels in supernatants of fibroblasts (CAF-1, CAF-2, and HMF). Data represent three separate experiments. *p <0.05, **p <0.01.

Figure 2. CAFs activate oncogenic signaling in TNBC cells. **(a)** Conditioned media of CAFs activated Akt and STAT3 in MDA-MB-231 cells and ERK1/2 and STAT3 in SUM159 as shown with the blots and the quantified results. Statistical comparison was done between TNBC cells stimulated with CAF-1 or CAF-2 conditioned media and its respective control group. *p<0.05 denotes statistically significant comparisons between stimulated and vehicle control TNBC cells. **(b)** Crizotinib (MET inhibitor) significantly downregulated oncogenic signaling in TNBC cell lines. The graphs show quantified phospho-protein levels normalized with total protein levels in TNBC cells when stimulated with conditioned medium from CAF-1, with or without MET inhibition (0.5 μM and 1 μM crizotinib). Statistical comparison was done between TNBC cells stimulated with CAF-1 conditioned medium and the stimulated TNBC cells under crizotinib treatment (One-way ANOVA followed by post-hoc test). Data represent two separate experiments with three replicates. *p<0.05.

Figure 3. Met activity in EGFR$^+$ TNBC. **(a)** Analysis of METABRIC breast cancer database (TCGA) shows that expression levels of both MET and EGFR genes are significantly higher in basal and claudin-low subtypes. **(b)** MET expression strongly correlates with EGFR expression both at a gene level (METABRIC breast cancer database TCGA) and at a protein level (Firehose Legacy breast cancer database, TCGA). **(c)** Analysis of functional proteomics data of tumors from patients with invasive breast cancer derived from TCPA database shows a strong correlation between p-MET and p-EGFR. *p<0.05, **p<0.01.

Figure 4. CAFs promote matrix invasion and proliferation of TNBC cells in an organotypic tumor model. **(a)** Two-step micropatterning approach to create a tumor model that consists of a TNBC cell mass within a stroma composed of ECM and dispersed CAFs. The images show confocal reconstruction of the tumor model. Left: TNBC mass (blue) and CAFs (green); Right: TNBC mass (green), CAFs (red), and collagen (cyan). Scale bar is 200 μm. **(b)** Confocal images of TNBC cells on day 5 of culture show that unlike HMFs, CAFs promote matrix invasion of MDA-MB-231 and SUM159 cells. **(c)** Normalized matrix invasion of MDA-MB-231 and SUM159 cells (n=8). **(d)** Flow cytometry results from organotypic tumor models with HMFs, CAF-1, or CAF-2 used as fibroblasts and TNBC cells. **(e)** Quantified cell proliferation results with absolute count of MDA-MB-231 and SUM159 cells. *p<0.05 and n=6.

Figure 5. CAFs promote EMT of TNBC cells. **(a)** TNBC cells in 3D organotypic culture with CAF-1 and CAF-2 show a mesenchymal morphology as quantified by elevated cell aspect ratio. **(b)** CAFs increase the expression of EMT gene markers in MDA-MB-231 and SUM159 TNBC cells in organotypic models. n=2 independent experiments, two replicates/experiment, *p< 0.05. **(c)** Both TNBC cell lines stimulated with conditioned medium from CAFs show elevated expression of EMT protein markers. n=2 with three replicates. *p< 0.05.

Figure 6. Cyclic drug treatment and recovery of MDA-MB-231:CAF-1 co-culture spheroid. **(a)** The co-culture spheroids were cyclically treated with an inhibitor of MEK (5 nM trametinib). **(b)** Kinetics of spheroids growth during the cyclic treatment and recovery regimen. Each data point in the line graph is an average of eight replicates. **(c)** Percentage viability of TNBC cells measured from fluorescence intensity of endogenous GFP signal of TNBC cells (n=8). **(d)** Growth rate (k_C) of co-culture spheroids during four treatment rounds with trametinib (n=8); *p<0.01. Error bars in panels (b-d) represent the standard errors from a mean value. **(e)** Activities of ERK1/2, Akt, and MET following T1 and T3 treatments of MDA-MB-231:CAF-1 co-culture spheroids with trametinib. The Control lane represents untreated spheroids.

Figure 7. Therapeutic targeting of CAFs-TNBC cell interactions in organotypic cultures. **(a,b)** Matrix-format dose-dependent combination treatments with crizotinib/trametinib against MDA-MB-231 and crizotinib/dactolisib against SUM159 cells (n=3). **(c,d)** Quantified inhibition of invasion of TNBC cells by the combination treatments. The boxed cells show highly synergistic combination pairs. **(e,f)** Quantified flow cytometry results with absolute counts of TNBC cells in free-floating spheroids, in organotypic cultures containing CAF-1 and TNBC cells (control), in organotypic cultures under single-agent treatments (+1 μM crizotinib or +5 nM trametinib with MDA-MB-231) and (+1 μM crizotinib or +1 μM dactolisib with SUM159), and in organotypic cultures under combination treatments (+crizotinib+trametinib with MDA-MB-231) or (+crizotinib+dactolisib with SUM159). *p<0.05 and n=5. **(g-i)** Effects of single-agent treatments with crizotinib and trametinib and their combination on activities of ERK1/2, Akt, and STAT3 signaling, gene expression of EMT transcription factors, and vimentin and N-cadherin proteins in MDA-MB-231 cells. **(j-l)** Effects of single-agent treatments with crizotinib and dactolisib and their combination on activities of ERK1/2, Akt, and STAT3 signaling, gene expression of EMT transcription factors, and vimentin and N-cadherin proteins in SUM159 cells. n=2 independent experiments, two replicates/experiment, *p< 0.05.

Fig 1

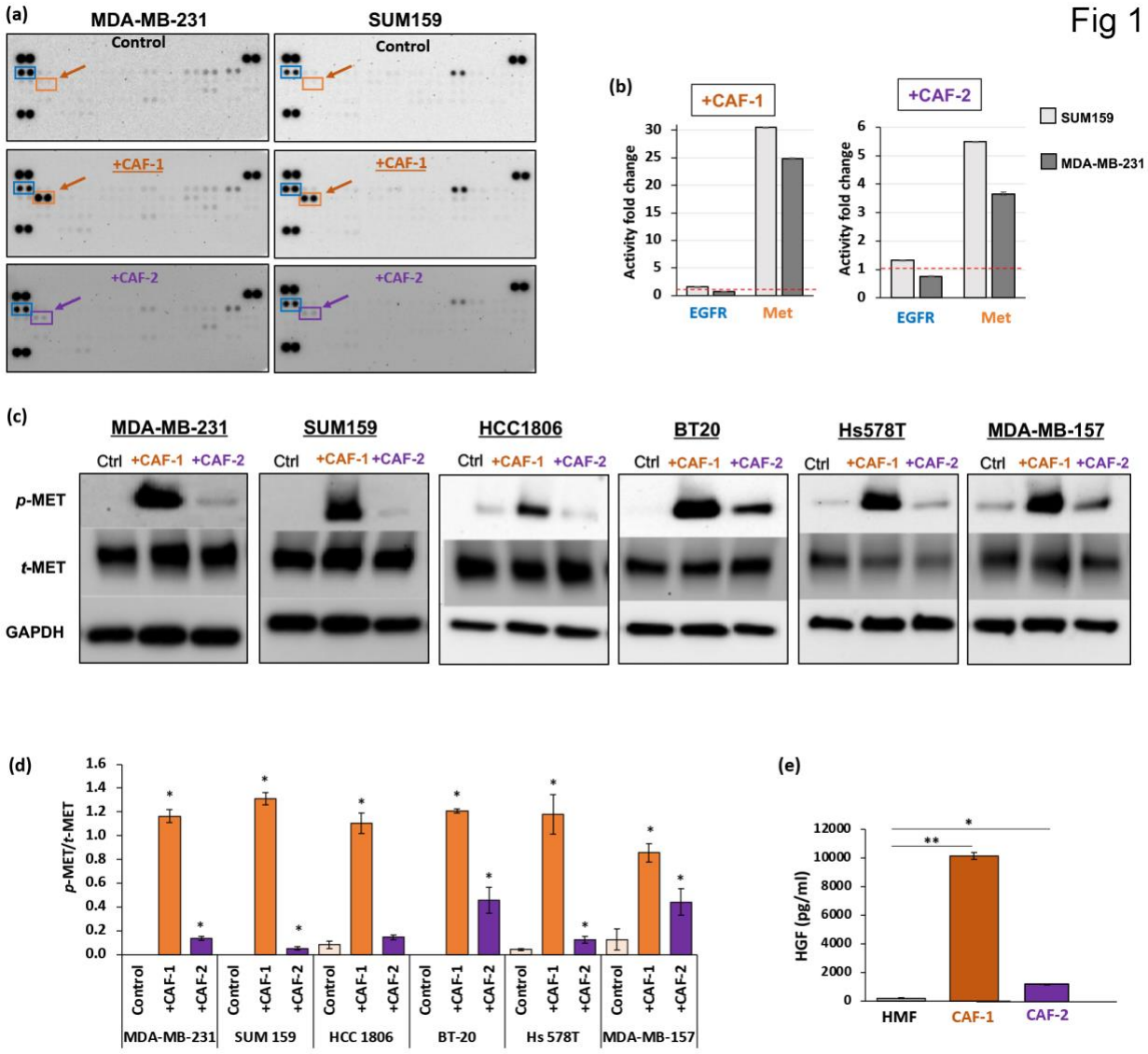
(a)
MDA-MB-231
SUM159
Control
+CAF-1
+CAF-2
(b)
+CAF-1
+CAF-2
SUM159
MDA-MB-231
Activity fold change
EGFR
Met
(c)
MDA-MB-231
SUM159
HCC1806
BT20
Hs578T
MDA-MB-157
Ctrl
+CAF-1
+CAF-2
p-MET
t-MET
GAPDH
(d)
p-MET/t-MET
Control
+CAF-1
+CAF-2
MDA-MB-231
SUM 159
HCC 1806
BT-20
Hs 578T
MDA-MB-157
(e)
HGF (pg/ml)
HMF
CAF-1
CAF-2

Fig 2

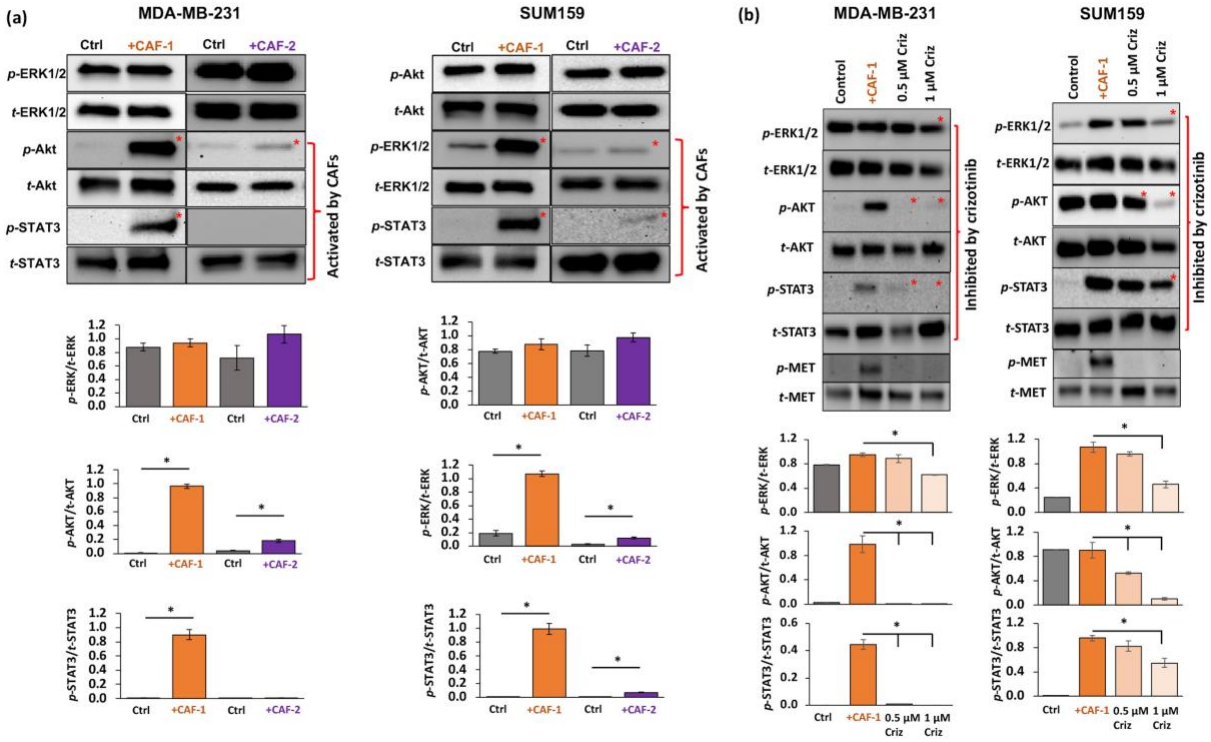
(a)
MDA-MB-231
SUM159
Ctrl
+CAF-1
+CAF-2
p-ERK1/2
t-ERK1/2
p-Akt
t-Akt
p-STAT3
t-STAT3
Activated by CAFs
p-ERK/t-ERK
p-AKT/t-AKT
p-STAT3/t-STAT3
(b)
MDA-MB-231
SUM159
Control
0.5 µM Criz
1 µM Criz
p-AKT
t-AKT
p-MET
t-MET
Inhibited by crizotinib

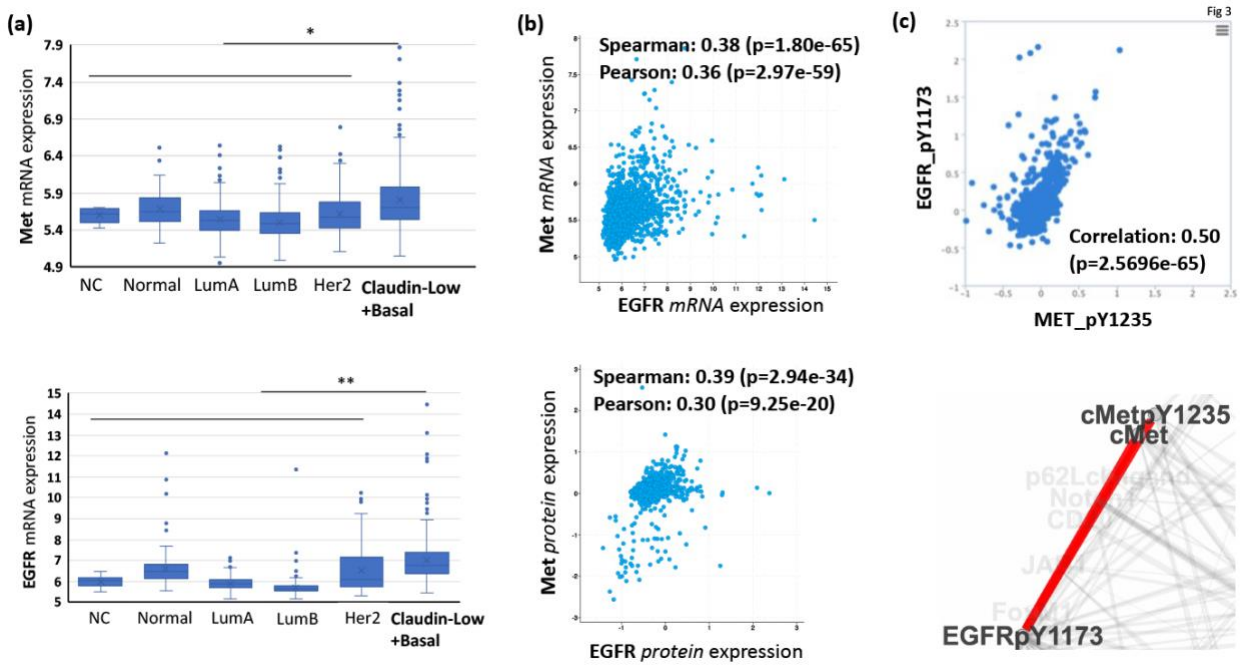
(a)
Met mRNA expression
7.9
7.4
6.9
6.4
5.9
5.4
4.9
*
NC
Normal
LumA
LumB
Her2
Claudin-Low +Basal
EGFR mRNA expression
15
14
13
12
11
10
9
8
7
6
5
**
NC
Normal
LumA
LumB
Her2
Claudin-Low +Basal
(b)
Spearman: 0.38 (p=1.80e-65)
Pearson: 0.36 (p=2.97e-59)
Met mRNA expression
EGFR mRNA expression
Spearman: 0.39 (p=2.94e-34)
Pearson: 0.30 (p=9.25e-20)
Met protein expression
EGFR protein expression
(c)
Fig 3
EGFR_pY1173
Correlation: 0.50
(p=2.5696e-65)
MET_pY1235
cMetpY1235
cMet
EGFRpY1173

Fig 4

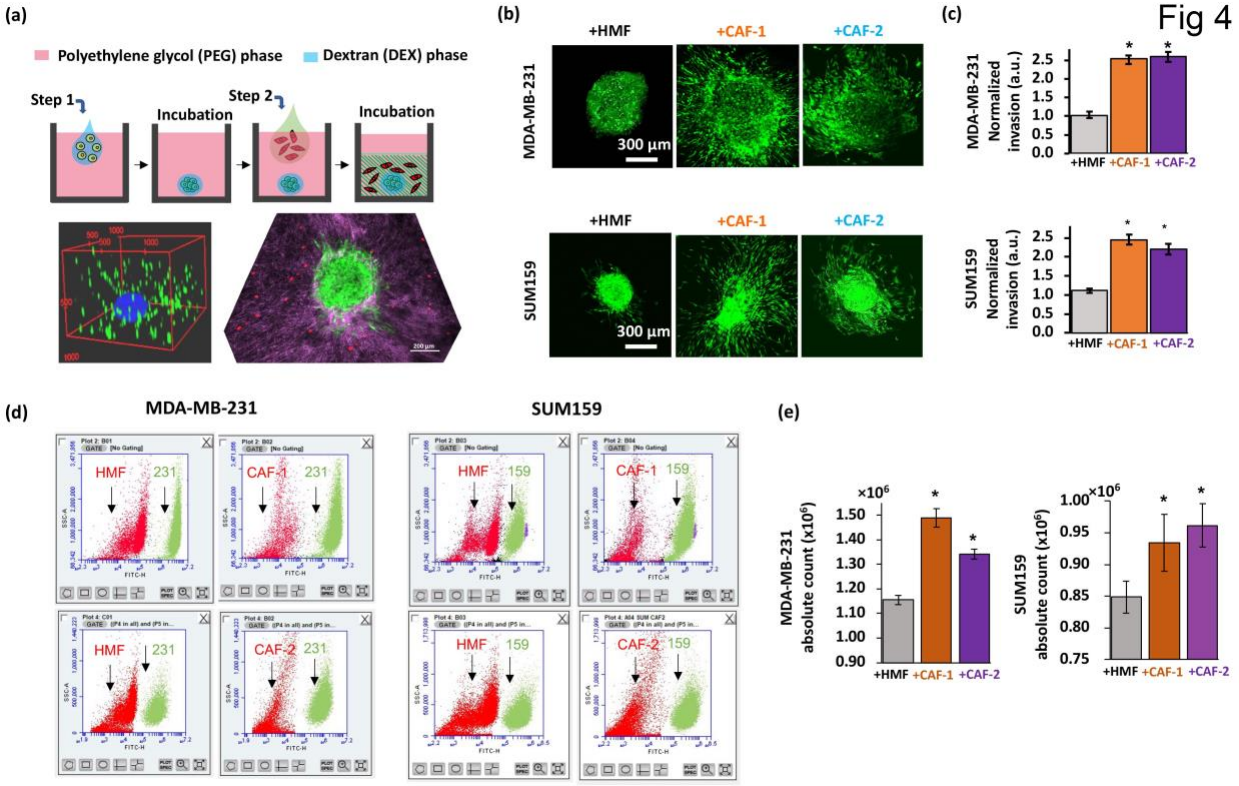
(a)
Polyethylene glycol (PEG) phase
Dextran (DEX) phase
Step 1
Incubation
Step 2
Incubation
(b)
+HMF
+CAF-1
+CAF-2
MDA-MB-231
300 μm
SUM159
300 μm
(c)
MDA-MB-231 Normalized invasion (a.u.)
SUM159 Normalized invasion (a.u.)
+HMF +CAF-1 +CAF-2
(d)
MDA-MB-231
SUM159
HMF
231
CAF-1
CAF-2
159
(e)
MDA-MB-231 absolute count (x10⁶)
SUM159 absolute count (x10⁶)
+HMF +CAF-1 +CAF-2

Fig 5

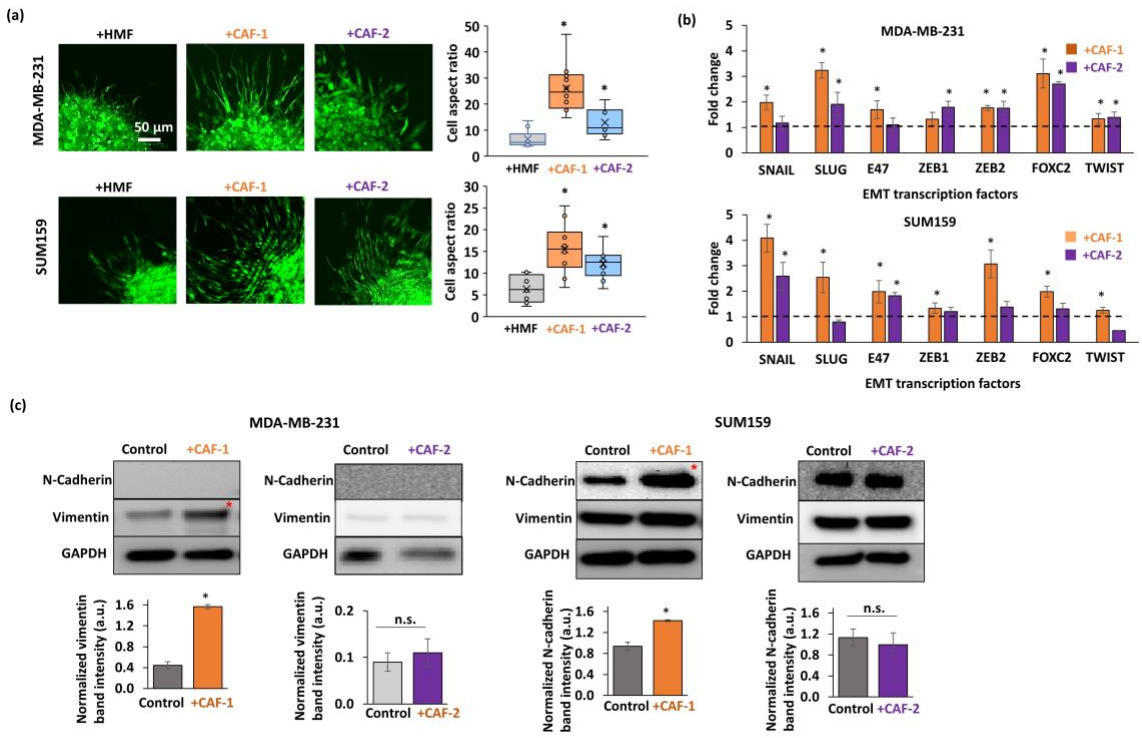
(a)
+HMF
+CAF-1
+CAF-2
MDA-MB-231
50 μm
SUM159
Cell aspect ratio
(b)
MDA-MB-231
Fold change
SNAIL
SLUG
E47
ZEB1
ZEB2
FOXC2
TWIST
EMT transcription factors
SUM159
(c)
MDA-MB-231
SUM159
Control
N-Cadherin
Vimentin
GAPDH
Normalized vimentin band intensity (a.u.)
Normalized N-cadherin band intensity (a.u.)
n.s.

Fig 6

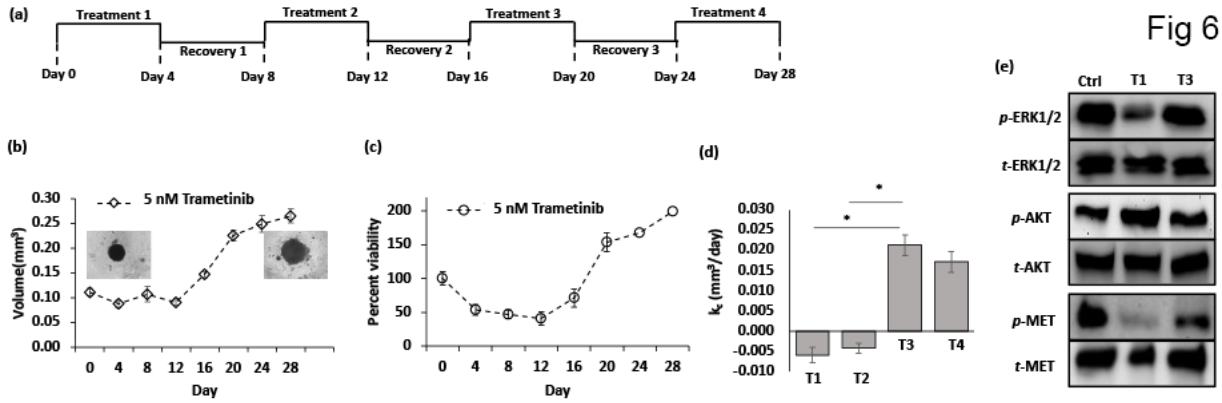
(a)
Treatment 1
Recovery 1
Treatment 2
Recovery 2
Treatment 3
Recovery 3
Treatment 4
Day 0
Day 4
Day 8
Day 12
Day 16
Day 20
Day 24
Day 28
(b)
5 nM Trametinib
Volume(mm³)
Day
(c)
5 nM Trametinib
Percent viability
Day
(d)
T1
T2
T3
T4
(e)
Ctrl
T1
T3
p-ERK1/2
t-ERK1/2
p-AKT
t-AKT
p-MET
t-MET

Fig 7

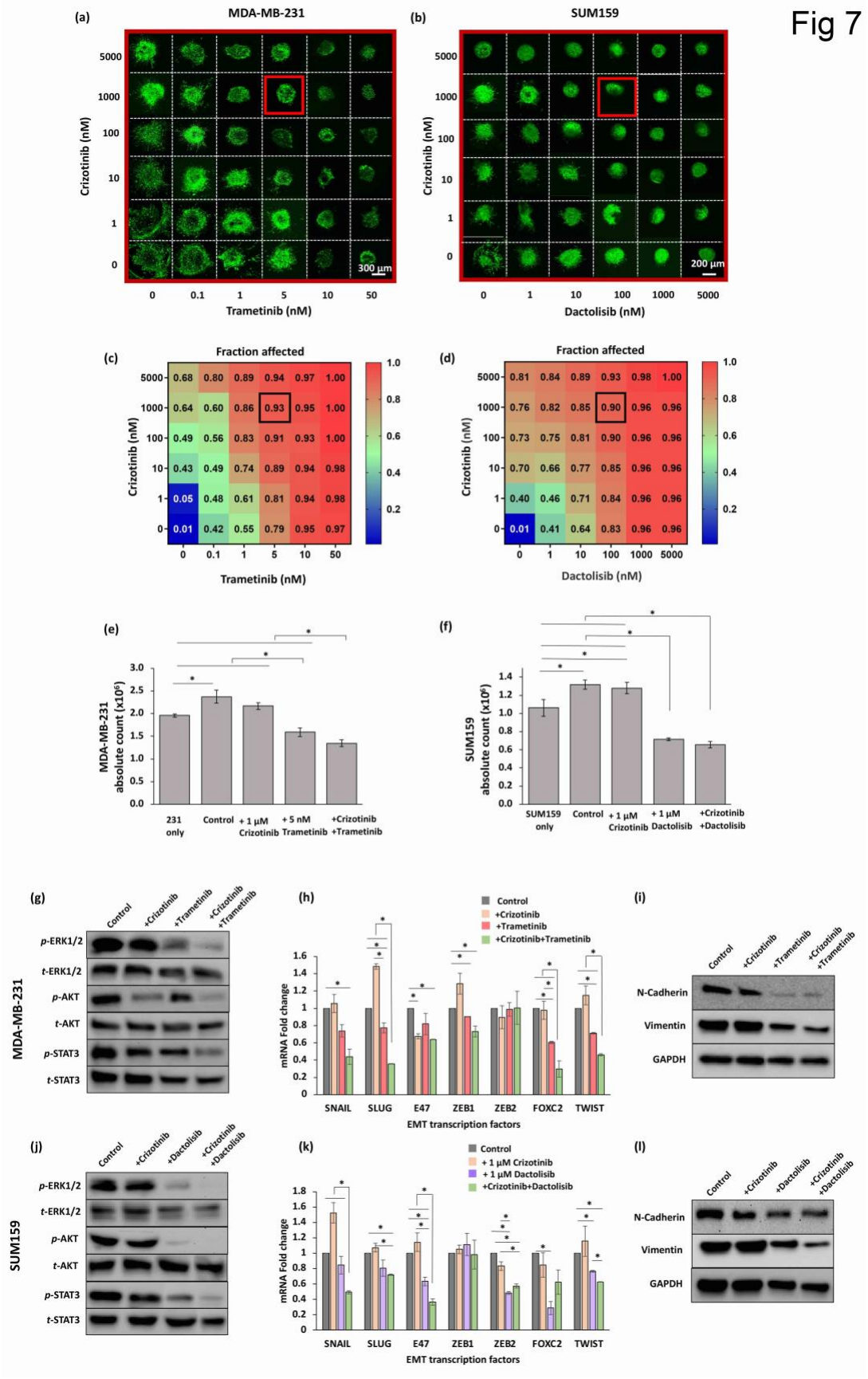
(a)
MDA-MB-231
Crizotinib (nM)
Trametinib (nM)
300 µm
(b)
SUM159
Dactolisib (nM)
200 µm
(c)
Fraction affected
(d)
(e)
MDA-MB-231 absolute count (x10⁶)
231 only
Control
+ 1 µM Crizotinib
+ 5 nM Trametinib
+Crizotinib +Trametinib
(f)
SUM159 absolute count (x10⁶)
SUM159 only
+ 1 µM Dactolisib
+Crizotinib +Dactolisib
(g)
MDA-MB-231
p-ERK1/2
t-ERK1/2
p-AKT
t-AKT
p-STAT3
t-STAT3
(h)
mRNA Fold change
SNAIL
SLUG
E47
ZEB1
ZEB2
FOXC2
TWIST
EMT transcription factors
(i)
N-Cadherin
Vimentin
GAPDH
(j)
SUM159
(k)
(l)